

PCCP

Accepted Manuscript



This is an *Accepted Manuscript*, which has been through the Royal Society of Chemistry peer review process and has been accepted for publication.

Accepted Manuscripts are published online shortly after acceptance, before technical editing, formatting and proof reading. Using this free service, authors can make their results available to the community, in citable form, before we publish the edited article. We will replace this *Accepted Manuscript* with the edited and formatted *Advance Article* as soon as it is available.

You can find more information about *Accepted Manuscripts* in the [Information for Authors](#).

Please note that technical editing may introduce minor changes to the text and/or graphics, which may alter content. The journal's standard [Terms & Conditions](#) and the [Ethical guidelines](#) still apply. In no event shall the Royal Society of Chemistry be held responsible for any errors or omissions in this *Accepted Manuscript* or any consequences arising from the use of any information it contains.

Crossover among structural motifs in Pd-Au nanoalloys

Beien Zhu,^{a,b,‡} Hazar Guesmi,^b Jérôme Creuze,^c Bernard Legrand^d and Christine Mottet^{e*}

Received Xth XXXXXXXXXXXX 20XX, Accepted Xth XXXXXXXXXXXX 20XX

First published on the web Xth XXXXXXXXXXXX 200X

DOI: 10.1039/b000000x

The crossovers among the most abundant structural motifs (icosahedron, decahedron and truncated octahedron) of Pd-Au nanoalloys are determined theoretically on a size range between 2 and 7 nm and for three compositions equivalent to Pd₃Au, PdAu and PdAu₃. The chemical ordering and segregation optimisation are performed with Monte Carlo simulations using semi-empirical tight-binding potentials fitted to *ab initio* calculations. The chemical configurations are then quenched by molecular dynamical simulations in order to compare their energy and characterize the equilibrium structure as a function of the cluster size. For the smaller sizes (around 300 atoms and less) the structures are also optimized at the electronic level within *ab initio* calculations in order to validate the semi-empirical potential. The predictions of the crossover sizes for the nanoalloys cannot be simply extrapolated from the crossover of the pure nanoparticles but implies stress release phenomena related to the size misfit between the two metals. Indeed, alloying extends the range of stability of the icosahedron beyond the one of the pure systems and the energy difference between decahedra and truncated octahedra becomes asymptotic around the sizes of 5-6 nm. Nevertheless, such equilibrium results should be modulated regarding kinetics considerations or possible gas adsorption in experimental conditions.

1 Introduction

Since the discovery of the catalytic activity of gold nanoparticles supported on oxide surfaces¹, Au-based alloys nanoparticles became attractive in order to elucidate the origin of the reactivity of gold². Pd-Au catalysts have been shown to be very efficient for various reactions³⁻⁶ and in particular in the CO oxidation^{7,8}. The understanding of the reactive mechanism requires to control the composition, structure and chemical ordering at the surface. Moreover, many experimental studies have shown that gas adsorption-induced surface segregation occurs at the Pd-Au surface^{4-7,9} during catalytic reactions, which is in good agreement with theoretical predictions on surfaces¹⁰⁻¹² or small clusters^{13,14}. Moreover, in the case of CO oxidation, it has been shown experimentally that the higher performance of the Pd-Au catalysts was reached under high CO pressure⁸ thanks to the Pd surface segregation and the formation of Pd-dimers or chains which are necessary for the O₂ dissociation, whereas remaining gold atoms enable CO

adsorption and desorption.

Within the hypothesis of vacuum condition, another question which has not been addressed up to now concerns the equilibrium structure and morphology of Pd-Au nanoparticles on a large range of size. Such question has been answered on quite small Pd-Au nanoalloys (less than 100 atoms)^{15,16} with various symmetries or on pure clusters on a large range of size^{17,18}, determining the crossover among structural motifs with high symmetry. Other studies focused on thermodynamical study of the equilibrium ordering of Pd-Au nanoalloys^{19,20}, but much less on the characterization of the most stable structure and morphology as a function of cluster size, up to many nanometers in size to be compared to most of the experimental results. Following a first study on the CoPt nanoalloys system²¹ where the TOh motifs was theoretically stabilized from 2-3 nm and above, we will study the crossover sizes among the most probable motifs for three compositions of the Pd-Au alloys: Pd₃Au, PdAu and PdAu₃. The results differ from the Co-Pt system and cannot be simply deduced from the equilibrium shape of the pure nanoparticles.

This paper is composed of five sections: starting with the present introduction, we then present the model and simulation methods, and a comparison between the SMA and DFT calculations for the smallest sizes (less than 300 atoms). In the third section, the crossovers among the different motifs are illustrated. The fourth section displays isotherms on each motif in order to detail the atomic structure and chemical configuration and to analyse the crossover in terms of stress release. The conclusions are resumed in the fifth section.

[‡]Present address: Division of Interfacial Water and Key Laboratory of Interfacial Physics and Technology, Shanghai Institute of Applied Physics, Chinese Academy of Sciences, Shanghai, 201800 China.

^a CNRS-LRS, UMR 7197, Laboratoire de Réactivité de Surface, Université Pierre et Marie Curie, 4 place Jussieu, 75252 Paris, France.

^b ICGM/MACS-UMR5253, 8 rue de l'Ecole Normale, F-34296 Montpellier, France.

^c Paris Sud University, ICMO/SP2M, UMR8182, 15 rue Georges Clémenceau, F-91405, Orsay, France.

^d SRMP-DMN, CEA Saclay, F-91191, Gif-sur-Yvette, France.

^e Aix Marseille Université, CNRS, CINAM UMR7325, Campus de Luminy, F-13288 Marseille, France.

2 Model and simulation methods

We performed Monte Carlo and quenched molecular dynamics simulations using a tight binding semi-empirical potential within the second moment approximation of the density of states (SMA potential). This many-body potential has been fitted to *ab initio* calculations within the density functional theory (DFT). Some of the smaller sizes of clusters (less than 300 atoms) have been also calculated within the DFT starting from the configuration optimized by Monte Carlo and quenched molecular dynamics simulations using the SMA potential.

The SMA potential is a semi-empirical method, fitted to bulk properties, which is able to give qualitative results on the crossover sizes among different structural motifs on a large size range. The method cannot predict the exact crossover size with precision but gives a reliable estimation of the sequence and the range of sizes of the transitions. For the smaller sizes where the potential is the less reliable, we used DFT calculations to check the SMA results.

2.1 DFT calculations

The DFT calculations are performed using the Vienna Ab initio Simulation Package (VASP) code and the projector augmented wave (PAW)^{22,23} interaction potential between the electrons and the ions. The exchange and correlation functional are either the local-density approximation (LDA)²⁴ or the generalized gradient approximation (GGA)²⁵. The Brillouin zone integration is performed with the Monkhorst-Pack scheme with k-point mesh comprising 12 subdivisions along each reciprocal lattice vector. The convergence criterion for the electronic self-consistent cycle is fixed to 10^{-6} eV and the geometry optimization is performed within the conjugate-gradient algorithm until the convergence of the force is less than 10^{-2} eVÅ⁻¹.

The values of the lattice parameters, the cohesive energies and the surface energies have been calculated for the two metals (Table 1). The lattice parameters and the surface energies are better reproduced by the LDA functional as compared to the experimental values so that we chose the LDA results to fit the SMA potential.²⁶ For the alloys, the permutation of one impurity in each metal and the dissolution enthalpies have been calculated in the two diluted limits²⁶ (Table 2). The dissymmetry between the two limits is in good agreement with the one observed within DFT-GGA calculations²⁷ and experimental values.²⁸ The calculated dissolution enthalpy are lower than the experimental one but they correspond to the disordered alloy whereas it is not clear if the experimental mixing enthalpy at 300 K corresponds to the ordered or disordered state because the experimental critical temperatures are not well defined in that system.²⁸

For the calculations on small clusters (section 2.4), the

Table 1 Lattice parameter, cohesive energy and surface energies of Pd and Au. The experimental values are taken from Kittel, *Introduction to solid state physics*, 8th ed., Wiley, New-York (2005) for lattice parameters (p. 20) and cohesive energy (p. 50), and De Boer et al., *Cohesion in metals*, North-Holland, Amsterdam (1988) p. 662, for surface energies.

| metal | a (Å) | E_{coh} (eV/at.) | $\gamma^{(100)}$ (eV/at.) | $\gamma^{(111)}$ (eV/at.) |
|-----------|-------|--------------------|---------------------------|---------------------------|
| Pd (LDA) | 3.85 | -4.98 | 0.95 | 0.74 |
| Au (LDA) | 4.08 | -4.24 | 0.65 | 0.50 |
| Pd (GGA) | 3.96 | -3.71 | 0.76 | 0.59 |
| Au (GGA) | 4.18 | -3.04 | 0.48 | 0.31 |
| Pd (exp.) | 3.89 | -3.94 | 0.94 | - |
| Au (exp.) | 4.08 | -3.81 | 0.78 | - |

Table 2 DFT-LDA permutation and dissolution enthalpies from Creuze *et al.*²⁶ compared to the experimental values in the two diluted limits of the mixing enthalpies at 300 K.²⁸

| (eV/at.) | Pd(Au) | Au(Pd) |
|----------------------------|--------|--------|
| ΔH^{perm} | 0.63 | -0.10 |
| ΔH^{dissol} | -0.11 | -0.26 |
| ΔH^{dissol} (exp.) | -0.20 | -0.38 |

Gamma point was used in the Brillouin-zone integration for all considered clusters and a cubic cell with the side of 3 nm was chosen to provide enough spacing between metal clusters in the neighboring repeated cells.

2.2 SMA potential

This potential derives from the tight binding model in the so-called second moment approximation (SMA)²⁹ where the attractive term reproduces the second moment of the density of state of the metal inducing a square root dependence with the neighboring atoms whereas the repulsive term is a pairwise Born Mayer potential. The potential energy at site i for an atom of type a is then written as follows:

$$E_i^a = - \sqrt{\sum_{j, r_{ij} < r_{ab}^c} \xi_{ab}^2 e^{-2q_{ab}(\frac{r_{ij}}{r_{ab}^0} - 1)}} + \sum_{j, r_{ij} < r_{ab}^c} A_{ab} e^{-p_{ab}(\frac{r_{ij}}{r_{ab}^0} - 1)} \quad (1)$$

where r_{ij} is the distance between the atom at site i and their neighbors at site j , r_{ab}^c is the cut-off distance and r_{ab}^0 is the first neighbor distance depending on the nature of the atoms, and p_{ab} , q_{ab} , A_{ab} , ξ_{ab} are four parameters (listed in Table 4) which are fitted to the DFT values (Table 1) of the cohesive energies, lattice parameters and elastic constants for the pure metals, and to the mixing energies in the diluted limits (Table 2). It is well known that the SMA potential underestimates the surface energies but not homogeneously. As a consequence, other pa-

parameterizations¹⁵ lead to underestimate the difference of the surface energies of the two elements, whereas such quantity is a driving force for surface segregation³⁰, and particularly in this system²⁶. Therefore in this study, the parameters of the pure elements have been fitted to reproduce the difference of the surface energies of the two elements as obtained by DFT calculations (cf. Table 1 and Table 3).³¹ Finally, a cut-off after the fourth neighbors distance r_{ab}^c is introduced which depends on the metal for the homoatomic interactions and we take the larger one for the heteroatomic interactions: $r_{ab}^c = \max\{r_{aa}^c, r_{bb}^c\}$.

Table 3 SMA potential values of the surface energies of Pd and Au

| metal | $\gamma^{(100)}$ (eV/at.) | $\gamma^{(111)}$ (eV/at.) |
|-------|---------------------------|---------------------------|
| Pd | 0.65 | 0.51 |
| Au | 0.35 | 0.26 |

Table 4 Parameters of the Pd-Au SMA potential

| $a-b$ | P_{ab} | q_{ab} | A_{ab} | ξ_{ab} |
|-------|----------|----------|----------|------------|
| Pd-Pd | 11.75280 | 2.87486 | 0.14352 | 1.88570 |
| Au-Au | 10.71890 | 4.09805 | 0.22043 | 1.97573 |
| Pd-Au | 11.23585 | 3.48645 | 0.21410 | 2.08060 |

This potential leads to mixing enthalpies of the ordered phases in good agreement with the experimental values at room temperature (see Table 5). However, as mentioned previously, we are not sure that these experimental mixing enthalpies at 300 K²⁸ correspond to the ordered phases in the experiments. A more detailed comparison between LDA, GGA and experimental results will be given in an upcoming study.

Table 5 Mixing enthalpies (in meV/at.) calculated with the Pd-Au SMA potential in the ordered phases (DO₂₂ for Pd₃Au and PdAu₃, and A₂B₂ for the PdAu) and compared with the experimental ones²⁸

| | Pd ₃ Au | PdAu | PdAu ₃ |
|------|--------------------|------|-------------------|
| SMA | -45 | -79 | -66 |
| Exp. | -50 | -80 | -75 |

2.3 Numerical simulations

We proceed with two types of simulations to get the comparison between the different motifs in Pd-Au nanoalloys. First, using Monte Carlo simulations in semi-grand canonical (S-GCMC) or canonical (CMC) ensemble, we optimize the chemical configuration on different motifs of high symmetry for the clusters: icosahedron (Ih), decahedron (Dh) or truncated octahedron (TOh). Starting from these structures with well defined symmetries¹⁷, we propose random atomic

exchanges (within CMC) or permutations (within S-GCMC) and small random atomic displacements around each atom. In the S-GCMC the difference between the two chemical potential remains constant and the concentration evolves toward the equilibrium concentration, whereas in the CMC, the concentration remains constant. In both simulations, the pressure, the temperature and the total number of atoms are constant. The Metropolis sampling insures to reach a Boltzmann distribution of the chemical configuration at equilibrium and finite temperature. At low temperature and concerning the atomic positions relaxation, the Metropolis algorithm is less efficient so we use quenched molecular dynamics to get the ground state at 0K.

2.4 Comparison between the DFT and SMA results for the smaller sizes (less than 300 atoms)

Because the SMA potential has been fitted to bulk properties, it is not so much reliable to determine the energy of very small clusters with a molecular state. So in that subsection we would like to compare the energies of these small systems (less than 300 atoms) calculated within the SMA potential, with the energies obtained with DFT calculations. Starting from the equilibrium configurations as obtained by the CMC optimization with the SMA potential, the ions positions have been further optimized within the DFT-LDA and -GGA calculations. The results are shown in the figure 1 for the pure clusters and in the figure 2 for the nanoalloys of composition 3/4-1/4. Instead of plotting the average energy per atom, we plotted the energetic quantity usually considered in the comparison of pure nanoclusters of different size¹⁷ and which can be extended to nanoalloys in such way³²:

$$\Delta = (E_N - N_{Au}E_{coh}^{Au} - N_{Pd}E_{coh}^{Pd})/N^{2/3}$$

where E_N is the total energy of the system of N atoms to which we subtract the cohesive energy E_{coh}^a of the N_a atoms of the metal a in order to determine an excess energy with respect to the bulk of the pure elements, divided by $N^{2/3}$ which roughly scales as the number of surface atoms. Such quantity is relevant in what concerns the pure systems where it emphasises the difference in surface energy and excess core energy of the different structures, but it is not the case for the nanoalloys where the mixing energy equal to the excess energy between the alloy with respect to the pure elements in their bulk is strongly attenuated when divided by $N^{2/3}$. However in this section we only pay attention to the comparison between the DFT and the SMA results. Concerning the crossover size we will use an other criterion detailed in the next section.

We first notice on Fig. 1 and Fig. 2 that the LDA and GGA are very similar except in the absolute value of Δ which is less important. Then we notice that the SMA potential gives good qualitative ordering stability between the different structures for gold systems (Fig. 1) and rich-gold nanoalloys (PdAu₃ in

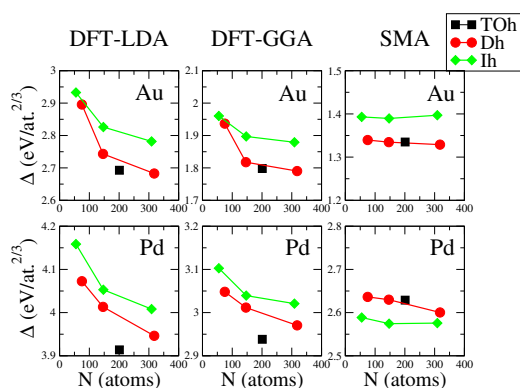


Fig. 1 Energy at 0K of the different motifs: Ih, Dh and TOh monometallic Pd and Au clusters calculated by DFT-LDA and -GGA, and with the SMA potential

Fig. 2). For Pd clusters, the SMA potential stabilizes the Ih at small sizes, whereas DFT stabilizes the TOh structure. In the SMA potential, the TOh and the Dh are degenerated. However, looking at larger sizes, the SMA potential finally stabilizes the Dh structure (Fig 3). For the Pd-rich nanoalloys, the difference between the two models are less important since the DFT calculations also favor the Ih of 55 and 147 atoms, as the SMA potential. The TOh₂₀₁ Pd₃Au nanoalloy in DFT is also more stable than in SMA potential.

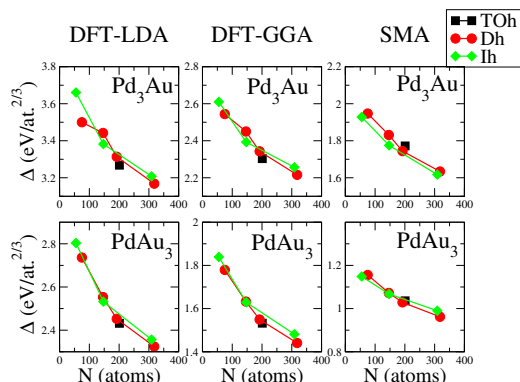


Fig. 2 The same as Fig. 1 for the nanoalloys of composition Pd₃Au and PdAu₃

As a conclusion, without the aim to determine some crossover size between the different motifs for such small clusters (less than 300 atoms) and also because the simple symmetries considered here are not representative of the most stable structures at these sizes^{15,16}, we simply conclude that our SMA potential is in good agreement with the DFT calculations for pure gold clusters and alloyed systems but fails to reproduce the DFT calculations for pure Pd ones and to a less extent for Pd₃Au ones. This gives a quite good level of con-

fidence for the results presented in the next section with the SMA potential concerning the crossover size among different motifs in nanoalloys, whatever the failing of the potential as compared to the DFT for the pure Pd small clusters.

3 Crossovers among different motifs

Before to consider the bimetallic systems, we first show on Fig. 3 the crossovers of the pure systems with high symmetry structures (Ih, Dh and TOh) as obtained in previous studies^{17,18}. The diameter of the nanoparticles is approximated by the following formula:

$$D = \frac{1}{2} \left(\frac{N}{4} \right)^{1/3}$$

where we consider that the number of atoms N is roughly proportional to the volume V of the nanoparticle of radius R so that $V = (4/3)\pi R^3 \sim 4R^3$ leads to $R \sim (\frac{N}{4})^{1/3}$. Then we take a coefficient equal to the average interatomic distance of 0.25 nm between R and $(\frac{N}{4})^{1/3}$ and $D = 2R$. This is a rough approximation of the nanoparticle diameter but we checked it was not so bad by measuring the exact diameter of some of the nanoparticles in this size range.

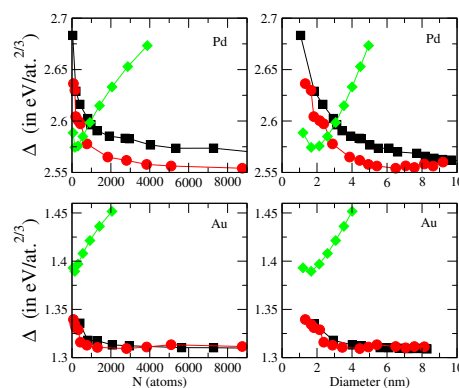


Fig. 3 Energy of the different high symmetry motifs (Ih, Dh and TOh) for pure Pd and Au clusters as a function of cluster size represented by the number of atoms N (left column) or the diameter D (right column) of the nanoparticle

We notice on Fig. 3 that for Pd clusters, the Ih is stable until size of 3 nm (about 1000 atoms), then Dh are stable between 3 and about 9 nm, after what the TOh should become stable but we did not extend more our calculations. This is completely different for the gold clusters since the Ih is never stable and Dh and TOh structures are almost degenerated.

The crossovers of the Pd-Au nanoalloys are illustrated on Fig. 4 where for a better clarity we plotted the difference in energy between the Ih or Dh structure and the TOh structure.

The crossover in nanoalloys appears at much larger sizes as compared to pure clusters. Indeed, when adding gold in palladium clusters, the Ih structure remains stable on a larger range of size, up to 6 nm (6000 atoms) as compared to less than 3 nm (1000 atoms) for pure palladium clusters. At equiconcentration of Au and Pd, the Ih is still stable until sizes of 3 nm (1000 atoms) and for rich-gold clusters, the Dh is stabilized for sizes smaller than 4 nm (2000 atoms).

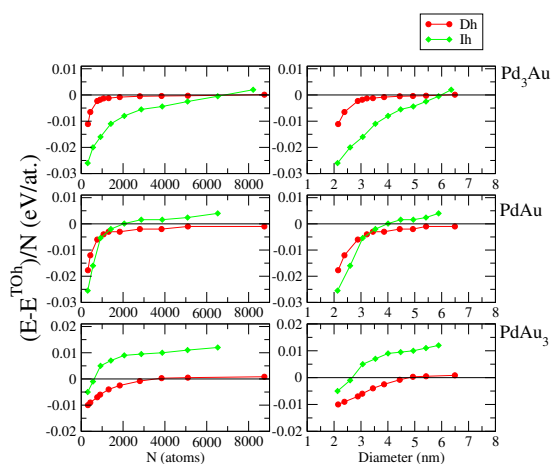


Fig. 4 Relative energy as referred to the TOh structure (zero energy) for the Ih and Dh motifs of Pd₃Au, PdAu and PdAu₃ compositions as a function of cluster size represented by the number of atoms N (left column) or the diameter D (right column) of the nanoparticle

The Ih structure is stabilized in nanoalloys on a larger range of size than in the pure systems of equivalent size. The Dh structure in nanoalloys converges toward the TOh structure at size about 3 nm (1000 atoms) for the composition Pd₃Au and PdAu. In the PdAu₃ systems, the convergence is delayed but the difference in energy remains very small (3 meV/at. at 4 nm i.e. for 2000 atoms). We can notice in that case that the TOh structure becomes favorable after sizes of 5 nm (4000 atoms).

These results cannot be deduced from a weighted average of the pure systems. For example, in the pure Au systems, the Dh has almost the same energy as the TOh whereas in the pure Pd systems Dh presents a lower energy than the TOh on a large range of size. However, in the rich-Au system, the Dh nanoalloys are more favorable than the same structure for the PdAu and the rich-Pd nanoalloys. Concerning the Ih nanoalloys, the range of stability of this structure is much larger as compared to the pure systems: however the tendency going from pure Pd to pure Au systems is respected. This means that the rich-Pd nanoalloys present the largest range of stability, then the PdAu nanoalloys, then the Au-rich ones.

We have no explanation to interpret the results concerning the relative stability of the Dh as compared to the TOh, but we will give some insights to illustrate the results of the Ih

nanoalloys in the next section. For that purpose, we will focus on the evolution of the stability of the Ih structure between pure metals and nanoalloys, especially looking at the chemical configurations, the surface segregation and core ordering using the segregation isotherms.

4 Segregation isotherms and internal stress

The chemical ordering and surface segregation are analyzed using S-GCMC in order to give a complete description of the chemical arrangement inside the nanoalloys Pd_{1-c}Au_c as a function of the Au concentration $c = c_{Au}$ for each motif: TOh₈₆₇₈, Dh₈₇₅₅ and Ih₆₅₂₅. We chose large sizes to give an average representation of the typical chemical arrangement for each motif.

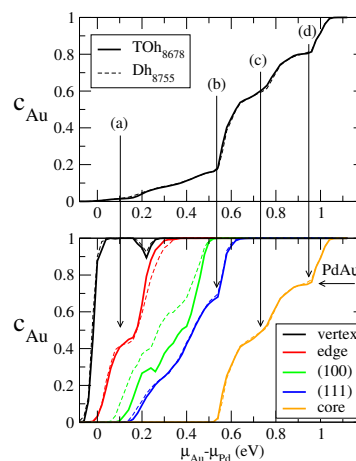


Fig. 5 Isotherms at 100 K for the TOh₈₆₇₈ and Dh₈₇₅₅ of Pd_{1-c}Au_c nanoalloys giving the global concentration (c_{Au}) (top) and the concentration on each type of sites: vertex, edge, (100) and (111) facets, and the core (bottom) as a function of the difference in chemical potential: $\mu_{Au} - \mu_{Pd}$; peculiar compositions (a), (b), (c) and (d) are illustrated on Fig. 6

The global concentration in gold (c_{Au}) and the surface concentration for each type of surface sites (vertex, edges, (100) and (111) facets) and the core concentration are plotted on Fig. 5, which gives an overview of the segregation isotherms at 100 K. First of all we can notice that the TOh and the Dh display almost identical isotherms, whatever their difference in atomic structure and morphology, except for the (100) facets where we notice a slight difference which concerns also a very small range of composition: less than 20% of gold.

An overall gold surface segregation is obtained in agreement with experimental results in vacuum conditions^{33,34} and

particular segregation at the edge is in good agreement with DFT calculations³³.

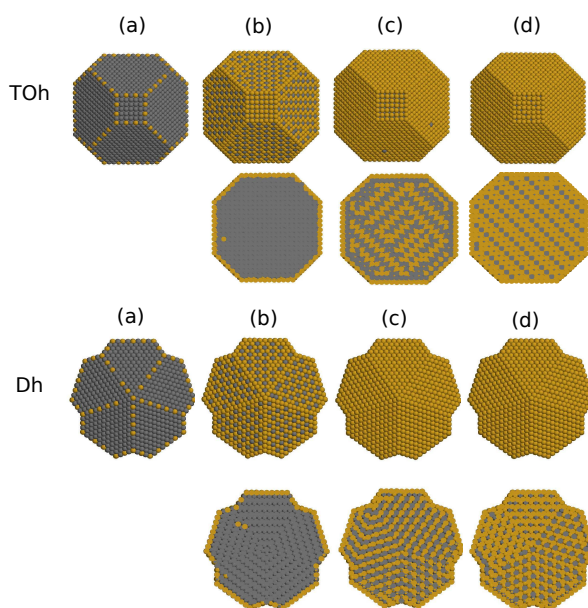


Fig. 6 Snapshots of the chemical configurations at 100 K of the TOh_{8678} and Dh_{8755} nanoalloys of $\text{Pd}_{1-c}\text{Au}_c$ corresponding to the peculiar compositions quoted on Fig. 5. Au atoms are represented in yellow and Pd atoms in grey.

It is worth noticing, secondly, that there is an important surface segregation sequence starting at the vertices, then on the edges, and then at the (100) and (111) facets. This leads to an almost perfect core/shell structure as can be seen on Fig. 6-(b), where only the (111) facets are not pure in gold. They are chemically ordered for a facet composition of about 66% of gold which corresponds to the $p(3\times 3)(111)$ superstructure in infinite surfaces. The ordering tendency leads to form mixed bonds where Pd atoms are surrounded by Au atoms inside the (111) facets. The surface segregation respects roughly the hierarchy of the broken bonds at the surface but there can be some interactions between the segregation on the different sites and some chemical ordering on each type of sites. For example we get a specific vertex and edge Au segregation where the ordering tendency of the alloy leads to alternate Au and Pd atoms along the edges and the vertices, corresponding to pure Au vertices and an almost equiatomic concentration on edges (Fig. 5 and Fig. 6-(a)).

Moreover, we notice that the isotherms display some irregularities which means that surface segregation and chemical ordering take place at given compositions at the surface and in the core. The illustrations of Fig. 6 correspond to the differ-

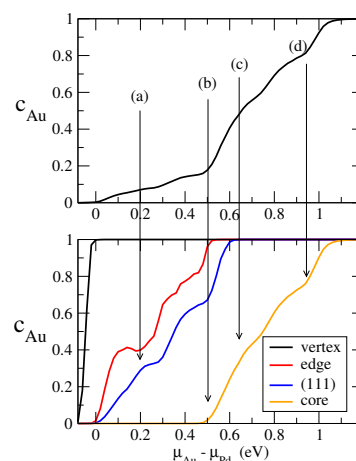


Fig. 7 Isotherms at 100 K of the Ih_{6525} nanoalloys of $\text{Pd}_{1-c}\text{Au}_c$ as in the Fig.5

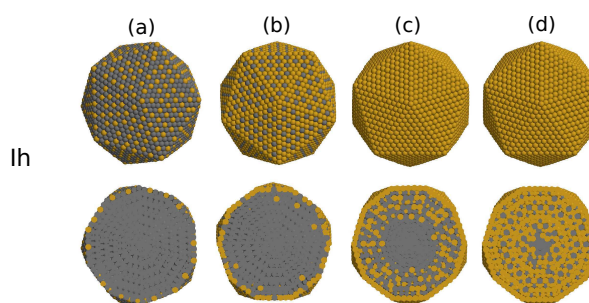


Fig. 8 Snapshots of the chemical configurations at 100 K of the Ih_{6525} nanoalloys of $\text{Pd}_{1-c}\text{Au}_c$ corresponding to the peculiar compositions quoted on Fig. 7

ent shoulders on the isotherms representing peculiar ordering on the edges (a), on the (111) facets as detailed before (b), but also inside the core for core compositions around 50% (c) and 75% of gold (d). In the case of the TOh structure, the core gets order following the A_2B_2 ordered phase at concentration around $c_{core}=0.50$ (but with defects) and following the DO_{22} around $c_{core}=0.75$, which are the phases of the bulk phase diagram obtained with the SMA potential³¹ and in good agreement with theoretical studies of ordering properties of Au-Pd alloys and nanoalloys¹⁹. We will not characterize here the ordering of the core with possible antiphase boundaries, which would need deeper analysis. In the case of the Dh structure, the core also gets order, but with a multitwinned structure composed of five slightly distorted tetrahedral units which share two by two one (111) face as twinning planes. We can notice locally ordered phases of the $L1_0$ type (c) or the $L1_2$ type (d) as compared to the A_2B_2 and DO_{22} ones in the TOh symmetry. We do not go deeper on the understanding of that chemical arrangement even if it raises interesting

questions but this will be performed in further studies.

The same isotherms at 100 K have been determined for the Ih_{6525} nanoalloys and are shown on Fig. 7. The overall shape of the global isotherm (global composition as a function of the difference in chemical potential) is not so different from the one of the Dh or TOh structures and the main characteristic is the almost core/shell structure with the gold segregation at the surface which corresponds to the weak slope at the beginning of the curve. However the surface of the Ih is different because there are only facets of the (111) type. There is the same shoulder on the edges as for the Dh or TOh structures, corresponding to the alternance of Pd and Au atoms along edges. More surprisingly, the edge concentration is then no more monotonic. It is probably related to their coupling with the concentration on these (111)-type facets. These facets present clearly two shoulders looking like "plateaus" roughly corresponding to the $p(3\times 3)(111)$ surface structure previously mentioned at 33% and 66% of gold. The corresponding structures are illustrated on Fig.8-(a) and (b) where the minority atoms are surrounded by the majority ones.

Then, there is a change in the slope of the isotherm corresponding to the core enrichment with gold, at the vicinity of the surface, as we can see on Fig.8-(b). The gold atoms are located near the surface, but not on the subsurface, which is in agreement with theoretical studies^{35,36} where the smaller atoms prefer to segregate at the subsurface. In Pd-Au system, the smaller atoms are the Pd atoms so that we get a Pd segregation at the subsurface. By increasing the gold concentration, the gold atoms are located exclusively in the neighborhood of the surface and not in the center of the Ih (see Fig.8-(c)), the center remaining pure in Pd even for high concentrations in gold (see Fig.8-(d)).

We have to recall here that the Ih structure is strongly compressed in its core, especially in its center, up to be relaxed by the introduction of a vacancy³⁷, or by an impurity with smaller atomic radius³⁸. Such stress relaxation also induced the equilibrium properties of so-called magic polyicosahedral core-shell clusters³⁹. More recently, a study related to the role of mechanical stress in the chemical ordering of Au-Pd nanoalloys has shown the influence of the stress on the chemical ordering in Ih²⁰.

We plotted on Fig.9 the local pressure on each concentric layer defined according to the variation of the energy as a function of a variation of the atomic volume⁴⁰:

$$p_i = -\frac{dE_i}{d\ln V_i} = -\frac{1}{3} \sum_j \frac{dE_i}{dr_{ij}} r_{ij}$$

where E_i is the energy at site i and r_{ij} the interatomic distance between the atom at site i and its neighbors at site j . This local pressure is converted in pressure units (GPa/at.) by dividing by an appropriate atomic volume. We can notice on Fig.9 that the pure Pd and Au Ih have the highest compression in the

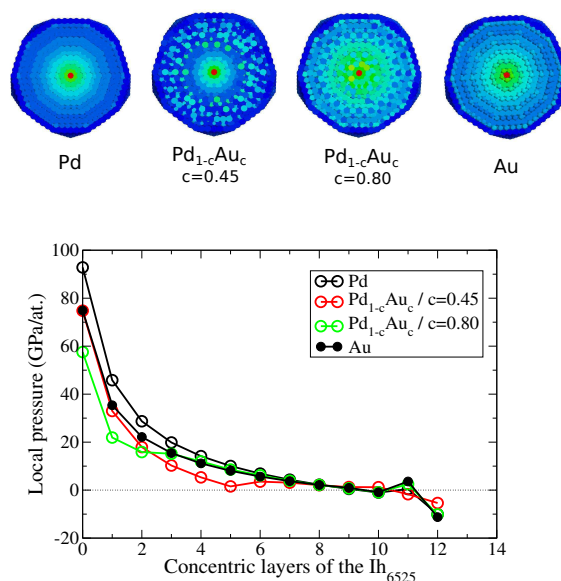


Fig. 9 Local pressure at 0 K of the Ih_{6525} nanoalloys of $Pd_{1-c}Au_c$ average on each atomic layer (in GPa/at.) as a function of the concentric layers of the Ih starting from its central atom (0) up to the surface (12); the snapshots give an illustration of the atomic pressure map of the nanoalloys with a color code going progressively from the deep blue color corresponding to the atoms in tension to the red color corresponding to the atoms in strong compression

center of the cluster, whereas by introducing 45% of gold in the Pd cluster, the stress is sensibly released from the center up to the sixth layer which means around half of the radius of the nanoparticle. This corresponds to the cluster represented in the Fig.8-(c). Then, going on to replace Pd atoms by gold atoms to reach the composition of 80% of gold (Fig.8-(d)), the stress is still more released in the very center of the Ih. The nanoalloy with 80% of gold, where Pd segregates to the center, has released the stress in the center as compared to pure gold Ih. So that finally the Ih nanoalloys tend to release locally the stress as compared to the pure systems.

This is also what we can conclude if we consider the total stress over each particle. Indeed, when we know how the stress is distributed inside the Ih between tensile zone at the surface and compressive zone in the core, we can ask how the total stress varies, knowing it should be globally equal to zero since there is no external pressure applied on the nanoparticle. In fact the residual total stress in the pure clusters is hundred times larger than the one in the nanoalloys: -4.64 GPa for the Pd Ih, -0.62 GPa for the pure Au Ih and only 0.04 and 0.02 for the 45% and 80% nanoalloys.

Following the argument that we can stabilize the nanoalloys by releasing of the mechanical stress energy, this gives an explanation to extend the range of stability of the Ih nanoalloys

structures as compared to their pure counterpart.

5 Conclusions

Using a semi-empirical SMA interatomic potential fitted to *ab initio* calculations, we determined for the first time the crossover sizes among different structural motifs on a large range of size: between 2 and 7 nm. Whereas the Ih structure is never stabilized in pure gold clusters and at very small sizes for pure Pd clusters (less than 3 nm or one hundred of atoms), the Ih structure is stable on a large range of size in Pd₃Au and PdAu nanoalloys (up to 6 nm for Pd₃Au and 3 nm for PdAu). This can be well explained regarding the core stress in the Ih structure which can be released by replacing large atoms by smaller ones in nanoalloys. The crossover sizes between Dh and TOh structures are not well defined and we rather obtain a convergence between the energies of these structures for Pd₃Au and PdAu nanoalloys. For the PdAu₃ systems, the crossover is reached after 5 nm. This is a first attempt to characterize the structure and morphology of Pd-Au nanoalloys on a large range of size to be compared to the experiments however such results may change in the presence of gas or by considering possible kinetics effects in experimental conditions.

Acknowledgments

We acknowledge support from the French Research National Agency under the Project ANR-11-JS07-0007, the EU COST Action MP0903, the the French HCP resources: CCRT/CINES/IDRIS under the allocations 2012[x2012086395] and 2013-096829. The first author also thanks for the development fund for Shanghai talents (Y439011011).

References

- 1 M. Haruta, *Gold. Bull.*, 2004, **37**, 27–36.
- 2 H. Zhang, T. Watanabe, M. Okumura, M. Haruta and N. Toshima, *Nature Materials*, 2012, **11**, 49–52.
- 3 M. S. Cheng, D. Kumar, C. W. Yi and D. W. Goodman, *Science*, 2005, **310**, 291–293.
- 4 L. Piccolo, A. Piednoir and J.-C. Bertolini, *Surf. Sci.*, 2005, **592**, 169–181.
- 5 A. Hugon, L. Delannoy, J. Krafft and C. Louis, *J. Phys. Chem C*, 2010, **114**, 10823–10835.
- 6 N. E. Kolli, L. Delannoy and C. Louis, *J. Catal.*, 2013, **297**, 79–92.
- 7 F. Gao, Y. Wang and D. W. Goodman, *J. Phys. Chem C*, 2009, **113**, 14993–15000.
- 8 F. Gao, Y. Wang and D. W. Goodman, *J. Phys. Chem C*, 2010, **114**, 4036–4043.
- 9 L. Delannoy, S. Giorgio, J. G. Mattei, C. R. Henry, N. E. Kolli, C. Mthivier and C. Louis, *ChemCatChem*, 2013, **5**, 2707–2716.
- 10 V. Soto-Verdugo and H. Metiu, *Surf. Sci.*, 2007, **601**, 5332–5339.
- 11 H. Guesmi, C. Louis and L. Delannoy, *Chem. Phys. Lett.*, 2011, **503**, 97–100.
- 12 A. Dhoubib and H. Guesmi, *Chem. Phys. Lett.*, 2012, **521**, 98–103.
- 13 P. S. West, R. L. Johnston, G. Barcaro and A. Fortunelli, *J. Phys. Chem C*, 2010, **114**, 19678–19686.
- 14 B. Zhu, G. Thrimurthulu, L. Delannoy, C. Louis, C. Mottet, J. Creuze, B. Legrand and H. Guesmi, *J. of Catalysis*, 2013, **308**, 272–281.
- 15 F. Pittaway, L. O. Paz-Borbon, R. L. Johnston, H. Arslan, R. Ferrando, C. Mottet, G. Barcaro and A. Fortunelli, *J. Phys. Chem. C*, 2009, **113**, 9141–9152.
- 16 A. Bruma, R. Ismail, L. O. Paz-Borbon, H. Arslan, G. Barcaro, A. Fortunelli, Z. Y. Li and R. L. Johnston, *Nanoscale*, 2013, **5**, 646–652.
- 17 F. Baletto, R. Ferrando, A. Fortunelli, F. Montalenti and C. Mottet, *The Journal of Chemical Physics*, 2002, **116**, 3856–3863.
- 18 C. Mottet, J. Goniakowski, F. Baletto, R. Ferrando and G. Tréglia, *Phase Transitions*, 2004, **77**, 101–113.
- 19 I. Atanasov and M. Hou, *Surf. Sci.*, 2009, **603**, 2639–2651.
- 20 B. Zhu and M. Hou, *Eur. Phys. J. D*, 2012, **66**, 63–71.
- 21 P. Andreatza, C. Mottet, C. Andreatza-Vignolle, J. Penuelas, H. C. N. Tolentino, M. De Santis, R. Felici and N. Bouet, *Phys. Rev. B*, 2010, **82**, 155453.
- 22 P. E. Blöchl, *Phys. Rev. B*, 1994, **50**, 17953–17979.
- 23 G. Kresse and D. Joubert, *Phys. Rev. B*, 1999, **59**, 1758–1775.
- 24 G. Kresse and J. Hafner, *Phys. Rev. B*, 1993, **47**, 558–561.
- 25 J. P. Perdew and Y. Wang, *Phys. Rev. B*, 1992, **45**, 13244–13249.
- 26 J. Creuze, H. Guesmi, C. Mottet, B. Zhu and B. Legrand, *submitted to Surf. Sci.*, 2015.
- 27 M. H. F. Sluiter, C. Colinet and A. Pasturel, *Phys. Rev. B*, 2006, **73**, 174204.
- 28 R. Hultgren, P. D. Desai, D. T. Hawkins, M. Gleiser and K. K. Kelley, *American Society for Metals, Metal Park, Ohio*, 1973.
- 29 V. Rosato, M. Guillopé and B. Legrand, *Phil. Mag. A*, 1989, **59**, 321.
- 30 J. Creuze, I. Braems, F. Berthier, C. Mottet, G. Tréglia and B. Legrand, *Phys. Rev. B*, 2008, **78**, 075413.
- 31 J. Creuze, B. Zhu, H. Guesmi, C. Mottet and B. Legrand, *in preparation*, 2015.
- 32 A. Rapallo, G. Rossi, R. Ferrando, A. Fortunelli, B. C. Curley, L. D. Lloyd, G. M. Tarbuck and R. L. Johnston, *J. Chem. Phys.*, 2005, **122**, 194308–194321.
- 33 H. L. Abbott, A. Aumer, Y. Lei, C. Asokan, R. J. Meyer, M. Sterrer, S. Shaikhutdinov and H.-J. Freund, *J. Phys. Chem. C*, 2010, **114**, 17099–17104.
- 34 A. R. Haire, J. Gustafson, A. G. Trant, T. E. Jones, T. C. Noakes, P. Bailey and C. J. Baddeley, *Surf. Sci.*, 2011, **605**, 214–219.
- 35 C. Langlois, Z. L. Li, J. Yuan, D. Alloyeau, J. Nelayah, D. Bochicchio, R. Ferrando and C. Ricolleau, *Nanoscale*, 2012, **4**, 3381–3388.
- 36 D. Bochicchio and R. Ferrando, *Phys. Rev. B*, 2013, **87**, 165435.
- 37 C. Mottet, G. Tréglia and B. Legrand, *Surf. Sci.*, 1997, **383**, L719–L727.
- 38 C. Mottet, G. Rossi, F. Baletto and R. Ferrando, *Phys. Rev. Lett.*, 2005, **95**, 035501.
- 39 G. Rossi, A. Rapallo, C. Mottet, A. Fortunelli, F. Baletto and R. Ferrando, *Phys. Rev. Lett.*, 2004, **93**, 105503.
- 40 P. C. Kelires and J. Tersoff, *Phys. Rev. Lett.*, 1989, **63**, 1164–1167.